Domínguez-Vázquez, A., Taccogna, F. y Ahedo, E. (2018). Particle modeling of radial electron dynamics in a controlled discharge of a Hall thruster. *Plasma Sources Science and Technology*, 27(6).

DOI: https://doi.org/10.1088/1361-6595/aac968

Particle modeling of radial electron dynamics in a controlled discharge of a Hall thruster

A Domínguez-Vázquez[1], F Taccogna[2] and E Ahedo[1]

[1] Universidad Carlos III de Madrid, 28911 Leganés, Spain
[2] CNR-NANOTEC—PLasMI Lab, via Amendola 122/D, 70126 Bari, Italy

E-mail: addoming@ing.uc3m.es

Abstract

An improved radial particle-in-cell model of an annular Hall effect thruster discharge with secondary-electron emission from the walls and a radial magnetic field is presented. New algorithms are implemented: first, to adjust the mean neutral density to the desired mean plasma density; second, to avoid the refreshing of axially accelerated particles; and third, to correctly weigh low-density populations (such as secondary electrons). The high-energy tails of the velocity distribution functions of primary and secondary electrons from each wall are largely depleted, leading to temperature anisotropies for each species. The secondary-electron populations are found to be partially recollected by the walls and partially transferred to the primary population. The replenishment ratio of the primary high-energy tail is determined based on the sheath potential fall. Significant asymmetries at the inner and outer walls are found for the collected currents, the mean impact energy, and the wall and sheath potentials. Radial profiles in the plasma bulk are asymmetric too, due to a combination of the geometric expansion, the magnetic mirror effect, and the centrifugal force (emanating from the $E \times B$ drift). The temperature anisotropy and non-uniformity, and the centrifugal force modify the classical Boltzmann relation on electrons along the magnetic lines.

Keywords: Hall thruster, particle-in-cell, secondary-electron emission

1. Introduction

The Hall effect thruster (HET) [1–3] is a mature technology, already widely and successfully used as both primary and secondary propulsion systems for a variety of space missions. In spite of its success, relevant physical phenomena of the plasma discharge inside the HET chamber and in its near plume are insufficiently known. This shortage drags out the development of new designs for new applications (for instance at low or high powers) and the optimization of existing devices. Also, it blocks the development of reliable and predictive simulation tools, which are considered essential, not only for design purposes, but also for accelerating tests of lifetime and of operation at different conditions (e.g. high thrust and high specific impulse).

One of the main open problems in HET research is related to plasma interaction with the thruster chamber walls and its effects on the electron velocity distribution function (VDF) and subsequent energy losses and plasma recombination at the walls. Due to the electric potential structure, the electrons are a confined population except for small currents that flow to the walls or downstream forming a plasma jet. This confinement would facilitate electron population thermalization, but the low collisionality of the discharge (at plasma densities of 10^{17}–$10^{18}\,\mathrm{m}^{-3}$) causes the VDF tails of electrons collected by the walls not to be fully replenished, and hence the VDF remains non-Maxwellian. A second issue, particularly acute for ceramics used in HET chambers, is the high secondary-electron emission (SEE) caused by the impact of 'primary' electrons from the plasma bulk. This SEE generates counterstreaming flows of secondary electrons [4–6] further making the VDF non-Maxwellian.

Ahedo and Parra [7] considered a one-dimensional planar (1Dp) stationary fluid model to analyze the plausible case where secondary electrons are partially trapped within the plasma bulk (and eventually thermalized) and partially recollected by the walls. They determined the effects of partial recollection on the potential fall in the sheaths (and its

charge saturation) and on energy flows to the walls. Later, Ahedo and dePablo [8] extended the analysis to the partial thermalization of both primary and secondary electrons with a 1Dp stationary kinetic model, describing the non-Maxwellian VDF and the SEE yields with phenomenological parameters. They obtained analytical expressions for the sheath potential fall and energy losses to the walls, in terms of the model parameters.

Sydorenko, Kaganovich, and coworkers [9, 10] treated a similar time-dependent 1Dp problem with a particle-in-cell (PIC) / Monte Carlo collision (MCC) formulation [11, 12]. Using a fixed background of neutrals, their steady-state solution confirmed the partial recollection of secondary electrons at the walls and, more importantly, determined the temperature anisotropy ratio of the VDF, in terms of the axial electric field, the collisional frequencies, and the SEE yields; interestingly, a near-wall conductivity effect [13] in the axial electron current was observed too. More recently, Wang *et al* [14] investigated, with a similar 1Dp PIC/MCC model, asymmetries in the electric potential profile and sheath potential falls caused by having different SEE yields at each wall (i.e. different materials).

Taccogna *et al* [15–17] considered a 1D radial (1Dr) PIC/MCC model, which is much more suitable for simulating a HET annular chamber and where asymmetry in the electric potential profile takes place naturally. The emphasis of these works is on the development of a strong asymmetry and a saturated stream instability propagating all along the radial domain, in conditions where a strong axial electric field induces an azimuthal electron drift of the order of the electron thermal speed.

The present paper revisits the model and code of Taccogna [16] with two types of goals. The first one is to enrich the numerical consistency and the capabilities of the code and, at the same time, to analyze the intrinsic limitations of 1Dp and 1Dr models. In this respect and even assuming azimuthal symmetry (i.e. $\partial/\partial\theta = 0$) the restriction of an axisymmetric (r, z) discharge to a given radial section ($z = \text{const}$) of the chamber implies that strong assumptions must be made on all terms related to the axial forces and plasma flows. As a consequence, there is a certain degree of arbitrariness on the 1D model that cannot be left aside when drawing conclusions on the model results. The second goal of the paper is to investigate further the steady-state solution (without stream instabilities) with focus on assessing the temperature anisotropy ratio of the VDFs of both primary and secondary electrons, combined with the asymmetries introduced by cylindrical geometry effects (which include geometrical expansion, centrifugal force, and the magnetic mirror). Finally, the influence of anisotropy and asymmetry on the macroscopic laws of interest is investigated.

The rest of the paper is organized as follows. The main physical aspects of the model are presented in section 2, while section 3 includes the numerical implementation and the validation of the new algorithms. A discussion of the main physical aspects of the plasma discharge is provided in section 4. Conclusions are drawn in section 5.

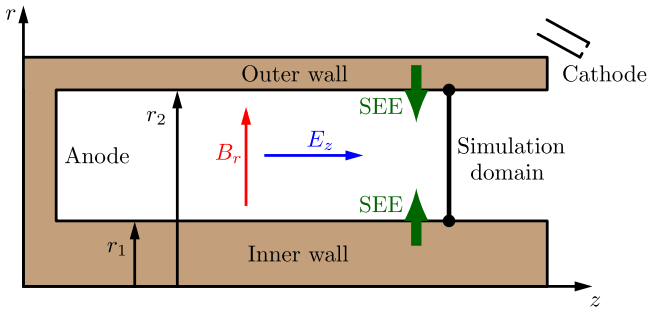

Figure 1. Sketch of a HET. The 1Dr simulation domain corresponds just to the thick black line.

2. The 1D radial model

The model analyzes the plasma radial structure at a given axial location within the acceleration region of a HET chamber, taking into consideration the weak plasma collisionality and the SEE from the walls due to the impact of energetic primary electrons. Figure 1 sketches the annular HET chamber with r_1 and r_2 as the inner and outer radii, respectively; $A = \pi(r_2^2 - r_1^2)$ is the area of the radial section.

The 1Dr model considers electrons e, singly-charged ions i, and neutrals n. Neutrals are modeled just as a spatially uniform population with a time-dependent density $n_\mathrm{n}(t)$ and a constant temperature T_n. Electrons and ions are modeled as two populations of macroparticles of constant weight W (i.e. the number of elementary particles per macroparticle) with densities and temperatures, n_j and T_j ($j = \mathrm{i}, \mathrm{e}$), evolving with ($r$,$t$). Let us define, representative of the instantaneous plasma density, the radially averaged electron density $\bar{n}_\mathrm{e}(t) = WN_\mathrm{p}/V$ where N_p/V is the number of macro-electrons per unit of volume.

We are interested here in simulating a quasi-stationary discharge with a certain mean plasma density, that is $\bar{n}_\mathrm{e}(t) \approx \text{const} = n_\mathrm{e0}$. In a 1D model, this requires one to make some decisions on the behavior of the particle sources and sinks. In a 1D cylindrical geometry, the conservation equations for ions and electrons reduce to

$$\frac{\partial n_j}{\partial t} + \frac{1}{r}\frac{\partial}{\partial r}(r n_j u_{rj}) = S_\mathrm{ioniz} + S_\mathrm{axial,}j, \quad j = \mathrm{i}, \mathrm{e}, \qquad (1)$$

where $n_j u_{rj}$ is the species radial flux; S_ioniz is the source term due to ionization, proportional to $n_\mathrm{n}(t)$; and $S_\mathrm{axial,}j$ is the source term due to the net axial contribution for species j. In a 2D (r, z) model one would have $S_\mathrm{axial,}j = \partial(n_j u_{zj})/\partial z$, but here $S_\mathrm{axial,}j$ is as arbitrary as the HET radial section we are attempting to simulate. In the quasi-steady state, the integral of the continuity equation over the plasma volume (expressed in electric current units) yields

$$I_\mathrm{wall,}j \approx I_\mathrm{ioniz} + I_\mathrm{axial,}j, \quad j = \mathrm{i}, \mathrm{e}, \qquad (2)$$

with $I_\mathrm{wall,}j$ denoting the species current lost into the wall, I_ioniz the (equivalent) current created through volumetric ionization (proportional to n_n and the same for electrons and singly-charged ions), and $I_\mathrm{axial,}j$ the current injected (or extracted) through the axial flow. While $I_\mathrm{wall,}j(t)$ is obtained directly

from the dynamic plasma response, different choices can be made on I_{ioniz} and $I_{\text{axial},j}$.

If $n_{\text{n}}(t)$ is known, then the plasma variables completely determine $I_{\text{ioniz}}(t)$, and the simulation of a stationary discharge requires $I_{\text{axial},j} \approx I_{\text{wall},j} - I_{\text{ioniz}}$. This implies a continuous injection (or extraction) of plasma from the domain, requiring one to define the properties of the injected macroparticles or the selection criteria for the extracted ones. We can distinguish between *axially controlled* discharge and *ionization-controlled* discharge (ICD) depending on whether $I_{\text{axial},j}$ is much stronger or much weaker than I_{ioniz}, respectively. In an axially controlled discharge, the plasma response is largely set by these conditions 'external' to the radial dynamics. Previous works seem to use $n_{\text{n}}(t) = n_{\text{n0}}$ and thus they operated in a mixed regime.

The present work implements a model for a fully ionization-controlled discharge with $S_{\text{axial,i}} = S_{\text{axial,e}} = 0$ and $n_{\text{n}}(t)$ adjusted in order that

$$I_{\text{ioniz}}(t) \approx I_{\text{wall},j}(t), \tag{3}$$

at any time. It will be shown that adjusting $n_{\text{n}}(t)$ is simple and it ensures that a stationary discharge is achieved. Besides, it corresponds reasonably to the physical situation in the HET chamber acceleration region, where ionization and wall recombination tend to compensate each other [6].

A 1Dr model needs also to prescribe the axial electric field E_z. This field accelerates the (nearly unmagnetized) ions over time, which is an undesirable secular effect on the 1Dr simulation. Previous works have dealt with this issue by occasionally resetting or refreshing the ion population. Here, we choose to just ignore the effect of E_z on the ions, which can be interpreted as a continuous axial refreshing of ions. Therefore, macro-ions are inserted initially or created later with a mean axial velocity u_{zi}, and they are subjected only to the radial electric field (and the magnetic field). Thus E_z affects electrons only, primarily by forcing with the magnetic field the electron $E \times B$ azimuthal drift. In fact, a key validation of the model will be to check that there is no secular increase of the macroscopic axial velocities of ions and electrons.

While E_z is taken to be constant and known, the radial electric field, $E_r = -\,\mathrm{d}\phi/\,\mathrm{d}r$, with $\phi(r, t)$ as the electric potential, satisfies the Poisson equation

$$\frac{\varepsilon_0}{r}\frac{\partial}{\partial r}\left(r\frac{\partial \phi}{\partial r}\right) = \rho_{\text{el}}(r, t), \tag{4}$$

with ρ_{el} denoting the net electric charge density of the plasma. The two boundary conditions for this equation are set here at the outer wall, $r = r_2$,

$$\phi_2 = 0, \quad \varepsilon_0 E_{r2} = -\sigma_2(t). \tag{5}$$

Here the first condition just sets a reference for the potential; ε_0 is the vacuum permittivity; σ_2 is the surface charge at the outer dielectric wall, to be defined in detail below; and the radial electric displacement of the dielectric wall is assumed to be negligible compared to $\varepsilon_0 E_{r2}$. A similar condition on E_{r1} is derived below in equation (9).

The magnetic field is assumed to be radial and, in order to be divergence-free, it satisfies

$$B_r(r) = B_{r1}\frac{r_1}{r}, \tag{6}$$

with B_{r1} known. Since $B_{r2}/B_{r1} = r_1/r_2 < 1$, magnetic mirror effects are possible.

Turning now to the plasma–wall interaction, ions and electrons reaching the walls are collected; however, ion recombination is not considered explicitly since neutrals are just modeled through $n_{\text{n}}(t)$. The SEE produced by the impacting electrons will follow the probabilistic model of [18]. In this model, the total SEE yield accounts for three different types of secondary electrons: backscattered ones (elastically reflected by the wall), rediffused ones (non-elas-tically reflected by the wall), and true secondary electrons (those extracted from the surface layers of the material). More details on the implementation of the SEE model are given in [16]. For the present purpose of better understanding the radial discharge and the electron VDF, backscattered and rediffused electrons are not considered, so that the SEE is limited to true secondary electrons. In the energy range of interest, the resulting SEE yield (i.e the true-secondary-to-primary flux ratio) reduces to

$$\delta_{\text{TS}}(E) \simeq E/E_{\text{c}} \tag{7}$$

with E denoting the impact electron energy, and E_{c} the crossover energy ($E_{\text{c}} = 51.1$ eV in simulations here [16]).

Simulations are generally started with a uniform electric potential profile. Thus, in a transient, the walls preferentially collect (highly mobile) electrons. These collected electrons build up a (negative) surface charge at the walls and create plasma Debye sheaths around them. The accumulation over time of the surface charge is determined from integrating the current conservation equation across the wall surface *and* over time:

$$\sigma_l(t) = -\int \mathrm{d}t \boldsymbol{j}_l(t) \cdot \mathbf{1}_l, \quad l = 1, 2. \tag{8}$$

Here l names the wall, $\boldsymbol{j}_l$ is the net electric current density at the plasma–wall boundary, and $\mathbf{1}_l$ is the wall normal pointing towards the plasma. At the steady state, $\boldsymbol{j}_l$ is zero for a dielectric and hence the surface charge remains constant.

As commented above, the integration of the Poisson equation across each of the wall surfaces yields

$$\varepsilon_0 E_{r2} = -\sigma_2(t), \quad \varepsilon_0 E_{r1} = \sigma_1(t), \tag{9}$$

if the electric displacement field of the dielectric is negligible. The first condition is already imposed as a boundary condition in equation (5). Consistency requires that the second one be satisfied automatically. This is indeed the case since the radial integration of the current conservation and Poisson equations yields

$$\varepsilon_0 [r E_r]_{r_1}^{r_2} = -\int [r j_r]_{r_1}^{r_2} \mathrm{d}t. \tag{10}$$

Table 1. Main input parameters including initial population settings, externally applied fields and grid definition. The magnitudes marked with an asterisk (*) are not input parameters of the model, but are derived from the other parameters instead. The variables named physical parameters are estimated from the other input values given at the initial conditions.

Type	Description	Symbol	Units	Value
Population settings	Number of elementary particles per macroparticle	W	—	$3 \cdot 10^9$
	Initial r-averaged plasma density	$\bar{n}_{e0}$	10^{17} m^{-3}	0.8
	Initial number of ion/electron macroparticles*	N_{p0}	—	106814
	Initial electron temperature	T_{e0}	eV	10
	Initial ion temperature	T_{i0}	eV	1
	Ion axial mean velocity	u_{zi}	km s^{-1}	10
	Initial background neutral density	n_{n0}	10^{17} m^{-3}	40
	Neutral temperature	T_n	K	700
***E*, *B* fields**	Electric field axial component	E_z	V cm^{-1}	100
	Magnetic field radial component at inner radius	B_{r1}	G	150
Simulation parameters	Inner radius	r_1	cm	3.5
	Outer radius	r_2	cm	5.0
	Number of nodes	N_r	—	1500
	Grid spacing*	Δr	μm	10
	Timestep	Δt	ps	5
Physical parameters	Debye length*	λ_D	μm	83.1
	Electron Larmor radius*	r_l	μm	802.0
	Inverse of plasma frequency*	$1/\omega_{pe}$	ps	62.7
	Inverse of electron cyclotron frequency*	$1/\omega_{ce}$	ps	379.1

The collisional processes implemented in the code are as follows: first, electron–neutral collisions including elastic scattering, excitation, and single ionization, following the models of [19–21]; and second, electron–ion, electron–electron, and ion–ion Coulomb collisions, according to the models of [22–25]. Ion–neutral collisions are found to be negligible for typical HET parameters.

In addition, we assume that secondary electrons are transferred to the main primary population when they undergo a collision with neutrals or a large-angle (greater than 90 degrees) Coulomb collision. Notice that, in a kinetic or particle formulation, the distinction between 'secondary' and 'primary' populations is just convenient for the analysis and understanding of the plasma response. In contrast, that distinction acquires full sense in multi-fluid electron models.

3. Numerical implementation and validation

The main input parameters and the resulting plasma magnitudes are listed in table 1. A uniform radial mesh of $N_r + 1$ points from r_1 to r_2 is chosen, with a cell size Δr smaller than the plasma Debye length λ_D. The electron and ion macroparticles have the same constant weight W throughout the simulation, chosen so that the initial number of both electron and ion macroparticles is $N_{p0} \approx 10^5$, corresponding here to about 70 macroparticles per cell. It has been checked in an independent simulation that using double this number of particles per cell reduces only the PIC fluctuations, without changing the averaged trends.

Xenon is assumed to be the propellant. The plasma macroscopic properties such as the particle densities and fluxes are computed at the mesh nodes through an area weighting algorithm [26]. The nodal weighting volumes are corrected according to [27]. Higher moments of the VDF, such as the temperature, are obtained for each simulated species through a new extended volumetric weighting algo-rithm presented in section 3.2. Additionally, surface weight-ing schemes [28, 29] are used for updating the particle fluxes to the walls.

In order to obtain the electric potential at the mesh nodes, second-order finite-difference schemes are used for discretizing

the Poisson equation along the radial coordinate r. The Thomas tridiagonal algorithm [30] is applied as a direct solving technique. The electron trajectories are propagated along time using both the radial and axial components of the electric field, and the radial magnetic field. In contrast, only the radial electric field is used to update the ions' velocity and position. The Boris–Buneman leapfrog algorithm [26] is applied to move all macroparticles one timestep forward considering the corresponding electric and magnetic fields interpolated to the macroparticles' position. The timestep is chosen so that $\Delta t < 0.3\omega_{\mathrm{pe}}^{-1}$, where ω_{pe} is the plasma frequency. This condition ensures the accurate integration of the electron gyromotion since $\omega_{\mathrm{pe}} > \omega_{\mathrm{ce}}$, with ω_{ce} denoting the electron gyrofrequency (see table 1).

After advancing all macroparticles by one timestep, the MCC module performs electron–neutral elastic and inelastic collisions. The constant timestep method of [19, 20] for selecting the type of collision is implemented using the cross sections from [31]. The probability distribution function for the progeny electrons generated by ionization is taken from [21]. A mean axial velocity $u_{z\mathrm{i}}$ is added to any newborn ion. Regarding the emission of true secondary electrons, a zero-drift semi-Maxwellian VDF with temperature $T_{\mathrm{eW}} = 2\,\mathrm{eV}$ is assumed.

3.1. The discharge control algorithm

An algorithm for an ICD with no axial contributions of plasma is presented here. In principle, there would be two methods to implement, both plotted in figure 2(a). The first one, used in previous works and represented by the dashed lines, fixes the neutral density, i.e. $n_{\mathrm{n}}(t) = n_{\mathrm{n0}}$ and lets the mean plasma density $\bar{n}_{\mathrm{e}}(t)$ evolve until a final state is reached after a few microseconds (i.e. a time related to the radial transit time of ions). The second method, represented by the solid lines of figures 2(a) and (b), fixes the mean plasma density in the domain, $\bar{n}_{\mathrm{e}}(t) \simeq \bar{n}_{\mathrm{e0}}$, and adjusts $n_{\mathrm{n}}(t)$ in order to satisfy equation (3).

In the first method the final plasma density is unknown and it can be very different from the initial one. For instance, the case of $n_{\mathrm{n}}(t) = 4 \cdot 10^{18}\ \mathrm{m}^{-3}$ starts with $\bar{n}_{\mathrm{e}} \approx 8 \cdot 10^{16}\ \mathrm{m}^{-3}$ and ends, after 25 μs, with $\bar{n}_{\mathrm{e}} \approx 6 \cdot 10^{15}\ \mathrm{m}^{-3}$. This implies that by starting with 80 macro-electrons per cell, we end with only 6 macro-electrons per cell, thus affecting the weighting accuracy. The advantage of the novel second method is that the number of macroparticles does not change practically along the simulation and thus it can be optimized before starting the simulation. Besides, it seems preferable to fix from the beginning the mean plasma density we are targeting to have, rather than the neutral density.

The second method is here implemented with the following ICD algorithm on neutrals. First, a tolerance is fixed for the variations of the average plasma density,

$$\epsilon_{c1} = |\bar{n}_{\mathrm{e}}(t)/\bar{n}_{\mathrm{e0}} - 1|. \tag{11}$$

Then, at every PIC–MCC timestep, both $\bar{n}_{\mathrm{e}}(t)$ and its rate of change $\Delta\bar{n}_{\mathrm{e}}$ are computed. The last one at instant k is defined as

$$\Delta\bar{n}_{\mathrm{e}}^{(k)} = \frac{1}{k_c}[n_{\mathrm{e}}^{(k)} - n_{\mathrm{e}}^{(k-1)} + (k_c - 1)\Delta\bar{n}_{\mathrm{e}}^{(k-1)}] \tag{12}$$

where $(k-1)$ and (k) are two subsequent instants of the PIC time and k_c is a fixed number of timesteps ($k_c = 100$ in the figures here).

The neutral density for instant $(k+1)$ is modified only if $|\bar{n}_{\mathrm{e}}(t)/\bar{n}_{\mathrm{e0}} - 1|$ is outside the above tolerance range, and

$$|\Delta\bar{n}_{\mathrm{e}}^{(k)}| > \epsilon_{c2}, \tag{13}$$

with ϵ_{c2} fixed. The reason for including a condition on the rate of change, $\Delta\bar{n}_{\mathrm{e}}$, is to filter fast oscillations and the numerical noise inherent in PIC calculations. Values of $\epsilon_{c1} = 10^{-3}$ and $\epsilon_{c2} = 10^{-2}$ have been found adequate to smoothly run the ICD algorithm here. The updated neutral density is defined as

$$n_{\mathrm{n}}^{(k+1)} = n_{\mathrm{n}}^{(k)} \frac{\bar{n}_{\mathrm{e0}}}{\bar{n}_{\mathrm{e}}^{(k)}}. \tag{14}$$

Figure 2(b) shows that the stationary discharge with $\bar{n}_{\mathrm{e}} \simeq 8 \cdot 10^{16}\ \mathrm{m}^{-3}$ requires $n_{\mathrm{n}} \approx 6.85 \cdot 10^{18}\ \mathrm{m}^{-3}$.

Figure 2(c) plots the evolution of the surface charges (in absolute value). In fact, the ICD algorithm is not applied until the surface charges $\sigma_f(t)$ are practically constant. This takes about 1 μs ($\sim 2 \cdot 10^5$ PIC timesteps) and corresponds to the formation time of the Debye sheaths (if the initial electric potential profile is flat). Figure 2(d) plots the evolution of the electric potential at the central point M (i.e. $r_{\mathrm{M}} = 42.5$ mm) for the ICD case and the non-ICD case with $n_{\mathrm{n}}(t) = n_{\mathrm{n0}}$.

Figures 2(e) and (f) detail the time evolution of partial currents for the ICD and the non-ICD cases, respectively. The net electric current to the two walls is there split into three populations: ions impacting the two walls (I_{wi}), electrons going *to* (and impacting) the walls (I_{wet}), and secondary electrons emitted *from* the walls (I_{wef}). The ICD case satisfies very well the steady-state and the dielectric conditions,

$$I_{\mathrm{ioniz}} = I_{\mathrm{wi}} = I_{\mathrm{we}}, \quad I_{\mathrm{we}} \equiv I_{\mathrm{wet}} - I_{\mathrm{wef}}, \tag{15}$$

(I_{we} is the net electron current to the walls) thus validating the ICD algorithm. In contrast, the non-ICD case satisfies the dielectric condition but there is a deficit in ionization. As a consequence, $\bar{n}_{\mathrm{e}}(t)$ and the currents to the walls decrease [see figures 2(a) and (f)]. As said before, the non-ICD simulation was run for 25 μs without reaching a steady state (or perhaps extinguishing), which anyway proves that a non-ICD procedure is not adequate.

3.2. The extended volumetric weighting algorithm

The PIC formulation operates with a constant macroparticle weight W for all the simulated species, which simplifies the treatment of collisional processes and saves computer memory. However, it also implies that, for each species, the number of macroparticles per cell is proportional to their density. The simulation parameters are optimized to accurately reproduce the response of the main species (ions and primary electrons) with similar densities (except inside the sheaths). But secondary electrons from the walls turn out to have a density one to two orders of magnitude lower. Thus, if

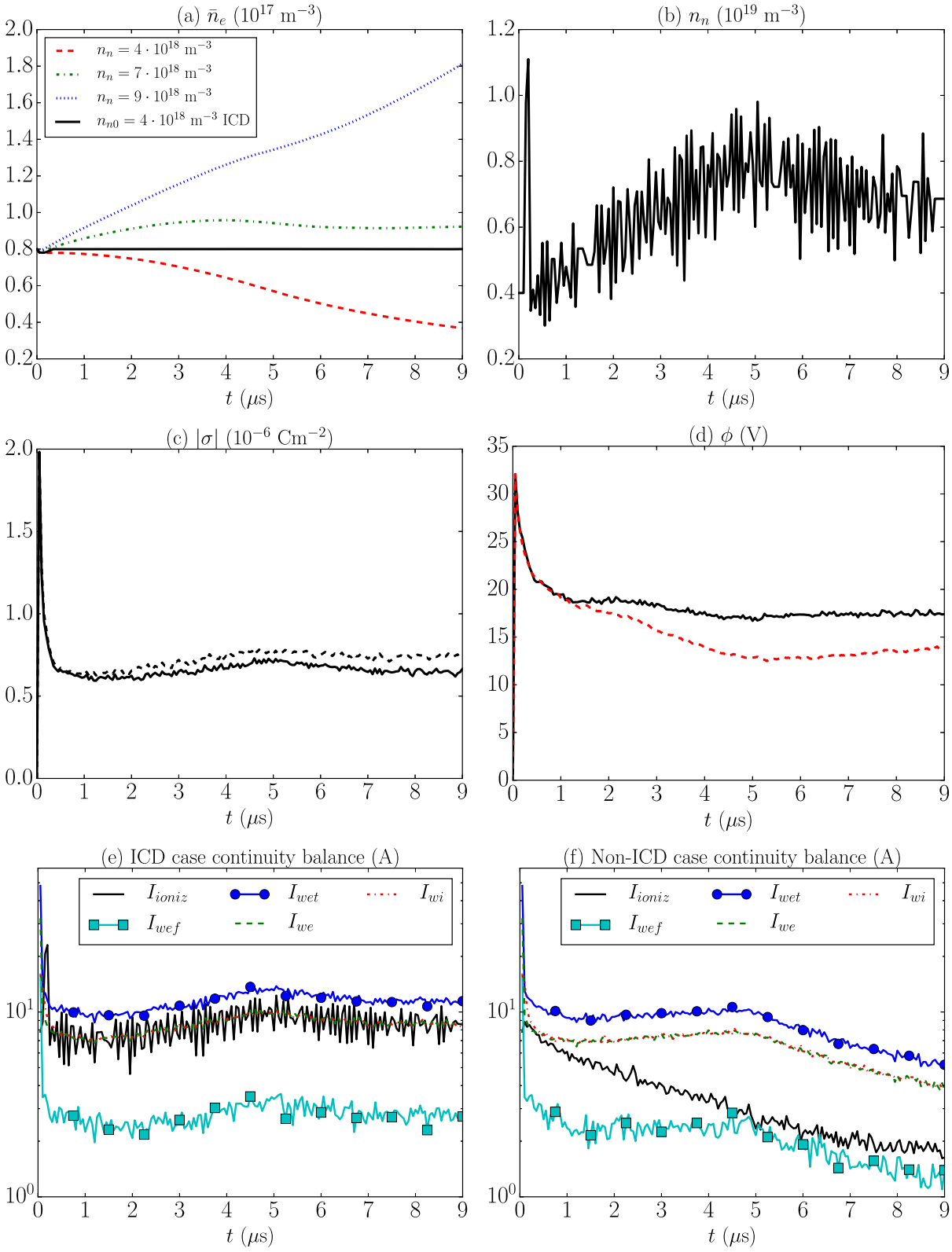

Figure 2. Time evolution of (a) the average electron density in the simulation domain for non-ICD (dashed) and ICD (solid) cases; (b) the background neutral density in the ICD case of the previous plot; (c) the absolute value of the surface charge densities at the inner (black solid) and outer (black dashed) walls in the ICD case; and (d) the electric potential at the central point M in the ICD case (black solid) and the non-ICD case with $n_{\mathrm{n}}(t) = n_{\mathrm{n}\ 0}$ (red dashed). Time evolution of the different electron sources and sinks on the current continuity balance of equation (15) for the ICD case (e) and the non-ICD case with $n_{\mathrm{n}}(t) = n_{\mathrm{n}\ 0}$ (f). All plots represent time-averaged magnitudes over $N_k = 10^4$ timesteps.

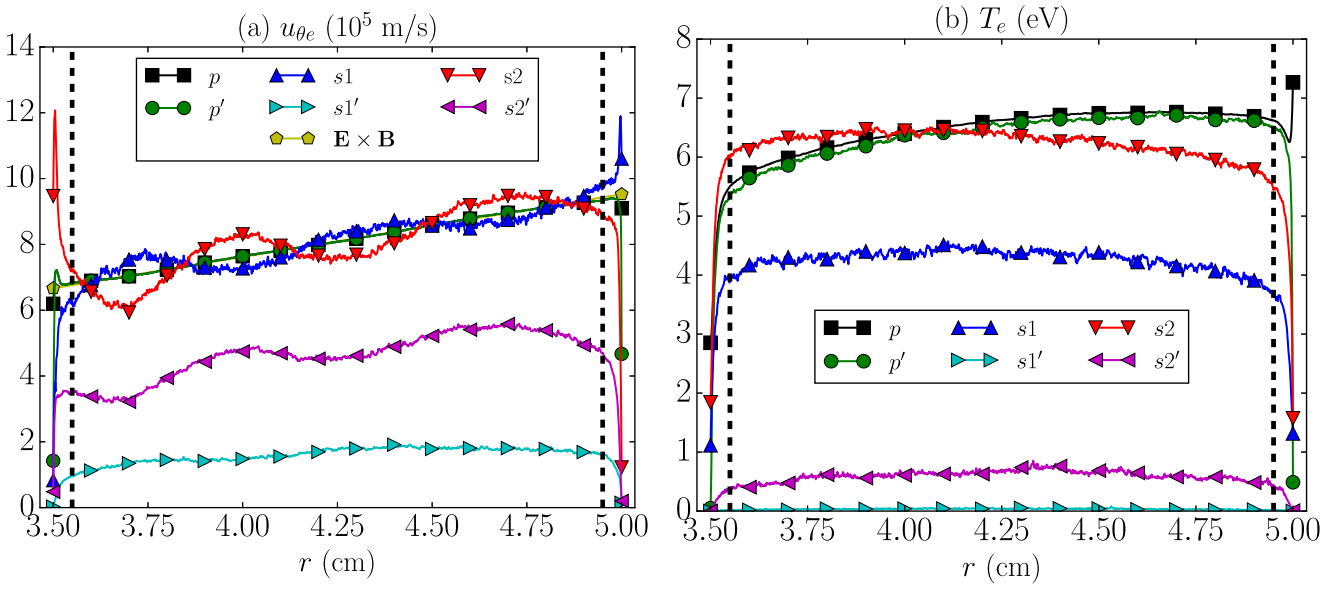

Figure 3. Steady-state radial profiles of (a) the macroscopic azimuthal velocities and (b) the mean temperatures of the different electron populations. Curves without (with) a prime correspond to extended (standard) volumetric weighting. Plot (a) also depicts the $E \times B$ velocity drift for comparison. The steady-state values are averaged over the last $N_k = 2 \cdot 10^5$ timesteps (equivalent to the last microsecond of simulation time). In both plots the vertical dashed lines represent the approximate inner and outer sheath edges.

there are 50–100 particles per cell for ions and primary electrons, there will be only 1–10 for secondary electrons. This leads to temporal oscillations on their density and, more importantly, to wrong estimates of their macroscopic velocity and temperature, as shown below.

This issue can be solved by extending in time the conventional volumetric weighting of the particles. The extended volumetric weighting (EVW) algorithm proposed here takes into consideration data from the last N_k timesteps. Thus the particle density of species j in a given node satisfies

$$n_j = \frac{W}{N_k \Delta V} \sum_k \sum_p s_p, \tag{16}$$

where ΔV is the weighting volume associated with the node, s_p is the weighting function assigning a weight to each macroparticle depending on its distance to the node, the sum in p is for all macroparticles with $s_p \neq 0$, and the sum in k is for the timesteps.

Similarly, the particle flux vector at the same node and time is given by

$$\boldsymbol{g_j} = \frac{W}{N_k \Delta V} \sum_k \sum_p \boldsymbol{v}_p s_p, \tag{17}$$

with $\boldsymbol{v}_p$ denoting the particle velocity. Then, the resultant fluid velocity is $\boldsymbol{u_j} = \boldsymbol{g_j}/n_j$. In the same way, the diagonal components of the pressure tensor at the same node and instant are computed as

$$p_{lj} = \frac{m\,W}{N_k \Delta V} \sum_k \sum_p (v_{lp} - u_{lj})^2 s_p, \quad l = r, \theta, z, \tag{18}$$

with m the mass of the elementary particle; the resultant temperatures are $T_{lj} = p_{lj}/n_j$.

Of course, the EVW filters oscillations of frequencies $(N_k \Delta t)^{-1}$ but this is not an issue when studying the steady-state discharge. For instance, in the simulations shown in this paper, values of $N_k = 10^4 - 10^5$ are taken, which correspond to 0.05–0.5 μs, so even oscillations of up to hundreds of kilohertz can be reproduced correctly.

Figure 3 plots the macroscopic azimuthal velocity and the mean temperature of the three electron species considered hereafter: primary electrons p, and (true) secondary electrons emitted by the inner s1 and outer s2 walls (recall that secondary electrons become primary electrons after a large-angle collision). In order to show the need for and the excellent performance of the EVW algorithm, these two macroscopic variables are plotted in two ways. The plotted EVW variables correspond to

$$\boldsymbol{u}_\mathrm{e} = \frac{\sum_k \sum_p \boldsymbol{v}_p s_p}{\sum_k \sum_p s_p}, \quad T_\mathrm{e} = \frac{m_\mathrm{e}}{3} \frac{\sum_k \sum_p |\boldsymbol{v}_p - \boldsymbol{u}_\mathrm{e}|^2 s_p}{\sum_k \sum_p s_p}. \tag{19}$$

The conventional volumetric weighting variables (averaged over N_k timesteps, to make the comparison fairer) correspond to

$$\boldsymbol{u}'_\mathrm{e} = \frac{1}{N_k} \sum_k \frac{\sum_p \boldsymbol{v}_p s_p}{\sum_p s_p}, \quad T'_\mathrm{e} = \frac{m_\mathrm{e}}{3N_k} \sum_k \frac{\sum_p |\boldsymbol{v}_p - \boldsymbol{u}'_\mathrm{e}|^2 s_p}{\sum_p s_p}. \tag{20}$$

Figure 3(a) shows that with EVW, the azimuthal velocities of the three electron populations well satisfy the $E \times B$ drift. In comparison, conventional weighting yields incorrect (too low) values of $u_{\theta \mathrm{e}}$ for secondary electrons. The reason for the discrepancies is that the instantaneous values used in equation (20) are weighted over a too small number of secondary macroelectrons per cell. Conventional weighting behaves well on $u_{\theta \mathrm{e}}$ for p-electrons since a sufficient number of macroparticles per cell are used at any timestep. Only near the walls there is some discrepancy between the two weightings on p-electrons, due

precisely to the decreasing density (and thus the decreasing number of macroparticles per cell) there.

The differences between the extended and conventional weightings are more pronounced when computing temperatures, since these variables measure velocity dispersion, so double summation on the particles per cell (both for $\boldsymbol{u}_j$ and for T_j) doubles the source of errors. In figure 3(b), conventional weighting works fine for the primary-electron temperature but it again underestimates much of the temperature of the secondary electrons; observe that it is practically zero for s1-electrons (and zero temperature is the natural value when there is only one particle per cell).

The vertical dashed lines in figure 3 approximately represent the edges of the Debye sheaths. Notice that a 'sheath edge' is well and exactly defined only in a two-scale asymptotic model applicable to the zero-Debye-length limit. In the present one-scale (i.e. nonzero Debye length) model, the definition of sheath edges is just meant for a more detailed analysis of the results, particularly to point out differences between the plasma responses at the plasma bulk and near the walls. We have located sheath edges at 0.5 mm ($\sim 6\lambda_D$) from the wall, based on data from the knees of the electric potential profile, the relative charge density, and the radial ion Mach number [see figure 5(c) below].

Observe that secondary electrons are born at the wall from a semi-Maxwellian VDF with $T_{eW} = 2$ eV. Then, within the Debye sheath, they are preferentially accelerated by the strong radial electric field E_r ($\sim 50\,000$ V m^{-1}), and enter the plasma bulk as a quasi-monoenergetic beam. Their effective magnetization (a cycloidal combination of azimuthal drift and gyromotion) takes place once they are inside the plasma bulk, within one Larmor diameter (~ 3 and ~ 4 mm, at the inner and outer sheath edges, respectively, based on the local magnetic field and radial velocity). The reproduction of this well-known behavior in the simulations can be considered as an important validation step.

It is worth pointing out that the EVW particle density defined in equation (16) is only used for macroscopic quantity calculation, while for solving the Poisson equation [equation (4)] instantaneous conventionally weighted electron and ion particle densities are considered so that any filtering effect due to the time-averaging process is avoided in the update of the ambipolar radial electric field.

4. Analysis of electron VDF and dynamics

The analysis here is focused on the stationary response for an ICD as defined in table 1. Table 2 compiles relevant data on the discharge that will be commented on in this section together with figures 4–6.

Figure 4(a) plots the radial profile of the self-adjusted electric potential. Points W_1, W_2, Q_1, Q_2, and M correspond to the walls, sheath edges, and channel mid-radius, respectively. The maximum potential is located just a bit inwards of point M and is only 0.03 V higher. The asymmetry of the potential profile due to cylindrical effects is evident at the sheath edges and the walls. The potential difference between the two sheath edges is $\Delta\phi_{Q_1Q_2} = 0.96$ V and that between the two walls is $\Delta\phi_{W_1W_2} = 2.27$ V. The latter is a bit higher than the typical emission energy of secondary electrons in our simulations, $T_{eW} = 2$ eV; nonetheless a simulation run with $T_{eW} = 0.2$ eV shows rather small differences in the steady-state response. A difference $\Delta\phi_{W_1W_2} > 0$ allows electrons emitted from wall W_2 to be recollected at wall W_1. However, there are two magnetic effects that change the perpendicular energy of electrons and therefore their radial energy and radial turning points (i.e. those with zero radial velocity, $v_r = 0$).

Neglecting collisions, the conserved total energy E of an electron satisfies

$$E = m_e \frac{v_r^2 + v_\perp^2}{2} - e\phi, \tag{21}$$

with $v_\perp$ as the non-radial component of the electron velocity. In the small electron Larmor radius limit, the phase-averaged perpendicular energy, $m_e v_\perp^2/2$, is the sum of the one due to gyromotion (which is proportional to the conserved magnetic moment μ) and the one due to the azimuthal $E \times B$ drift. Thus, here the radial kinetic energy satisfies

$$\begin{aligned} m_e \frac{v_r^2}{2} &\simeq E + e\phi - \mu B - W_d \\ &= E + e\phi(r) - \mu B_1 \frac{r_1}{r} - W_{d1} \frac{r^2}{r_1^2}, \end{aligned} \tag{22}$$

where $W_d = m_e E_z^2 / 2B_r^2$ is the gyrocenter azimuthal energy, and the rightmost side makes explicit the variation of B and W_d with r; in our simulations $W_{d1} = 1.27$ eV and $W_{d2} = 2.58$ eV at the inner and outer walls, respectively. Therefore, the radial energy of an electron moving inwards is decreased by the magnetic mirror and is increased by a change in the $E \times B$ drift. For the plotted simulation, the change in W_d is mild, but not negligible, compared to the change of ϕ in the plasma bulk. Later, in figure 6(b) it will be seen that this azimuthal energy plays a significant role in the electron macroscopic energy/momentum balance.

Figures 4(b)–(d) show the VDFs, $f_r(v_r)$, (once integrated over v_θ and v_z) of the primary and secondary electrons, p, s1 and s2, at points M, Q_1 and Q_2. Observe first that, in the plasma bulk, between Q_1 and Q_2, the densities of secondary electrons are much lower than those of primary electrons, n_p, so the latter determines almost exclusively the electric potential profile. In figures 4(b)–(d), solid vertical lines approximately (and in the absence of collisions) separate the central region of confined electrons from the left and right regions of electrons to be collected by the inner and outer walls, respectively. These lines correspond to the radial turning points from equation (22) for electrons with an average gyroenergy value of $\langle \mu B \rangle = 9.2$ eV.

Table 2 shows that the Coulomb collisions are negligible compared to the collisions with neutrals, but even the elastic electron–neutral frequency, ~ 3.7 MHz, is low compared with the transit frequency, ~ 62 MHz. This explains that the VDFs at point M, figure 4(b), present a large depletion of the high-energy

Table 2. Main parameters characterizing the steady-state discharge. Values averaged over the last microsecond of simulation time are used.

Type and units	Description	Symbol	Value
Electric potentials (V)	At the mid-radius M	ϕ_{M}	17.47
	At the inner sheath edge Q_1	$\phi_{\mathrm{Q_1}}$	13.70
	At the outer sheath edge Q_2	$\phi_{\mathrm{Q_2}}$	12.74
	At the inner wall W_1	$\phi_{\mathrm{W_1}}$	2.27
	At the outer wall W_2	$\phi_{\mathrm{W_2}}$	0.0
Collision frequencies (MHz)	e–n elastic collision	$\nu_{\mathrm{en}}^{\mathrm{el}}$	3.680
	e–n excitation collision	$\nu_{\mathrm{en}}^{\mathrm{ex}}$	0.209
	e–n ionization collision	$\nu_{\mathrm{en}}^{\mathrm{ion}}$	0.168
	e–i Coulomb collision	$\nu_{\mathrm{ei}}^{\mathrm{Coul}}$	0.076
	e–e Coulomb collision	$\nu_{\mathrm{ee}}^{\mathrm{Coul}}$	0.017
	i–i Coulomb collision	$\nu_{\mathrm{ii}}^{\mathrm{Coul}}$	0.119
Conversion to p and wall collection fractions (%)	s1 conversion to p	—	63.2
	s1 collection at the inner wall	—	7.5
	s1 collection at the outer wall	—	29.3
	s2 conversion to p	—	60.1
	s2 collection at the inner wall	—	28.7
	s2 collection at the outer wall	—	11.2
Current densities (A m^{-2})	p to the inner wall	$\lvert j_{\mathrm{p},1-}\rvert$	12.80
	s1 to the inner wall	$\lvert j_{\mathrm{s1},1-}\rvert$	0.17
	s1 from the inner wall	$\lvert j_{\mathrm{s1},1+}\rvert$	2.36
	s2 to the inner wall	$\lvert j_{\mathrm{s2},1-}\rvert$	2.96
	p to the outer wall	$\lvert j_{\mathrm{p},2+}\rvert$	23.97
	s1 to the outer wall	$\lvert j_{\mathrm{s1},2+}\rvert$	0.48
	s2 to the outer wall	$\lvert j_{\mathrm{s2},2+}\rvert$	0.81
	s2 from the outer wall	$\lvert j_{\mathrm{s2},2-}\rvert$	7.23
Mean impact energies per elementary particle (eV)	e ≡ p + s1 + s2 at the inner wall	$E_{\mathrm{we},1}$	8.10
	p at the inner wall	$E_{\mathrm{wp},1}$	8.50
	s1 at the inner wall	$E_{\mathrm{ws1},1}$	4.06
	s2 at the inner wall	$E_{\mathrm{ws2},1}$	6.59
	e ≡ p + s1 + s2 at the outer wall	$E_{\mathrm{e},2}$	15.75
	p at the outer wall	$E_{\mathrm{wp},2}$	16.16
	s1 at the outer wall	$E_{\mathrm{ws1},2}$	6.24

Table 2. (Continued.)

Type and units	Description	Symbol	Value
Electron energy balance source and sink terms (W)	s2 at the outer wall	$E_{ws2,2}$	9.34
	Electric field work	P_{elec}	337.67
	SEE energy gain	$P_{wall,f}$	5.56
	Wall losses	$P_{wall,t}$	153.40
	Inelastic collision losses	P_{inel}	194.30

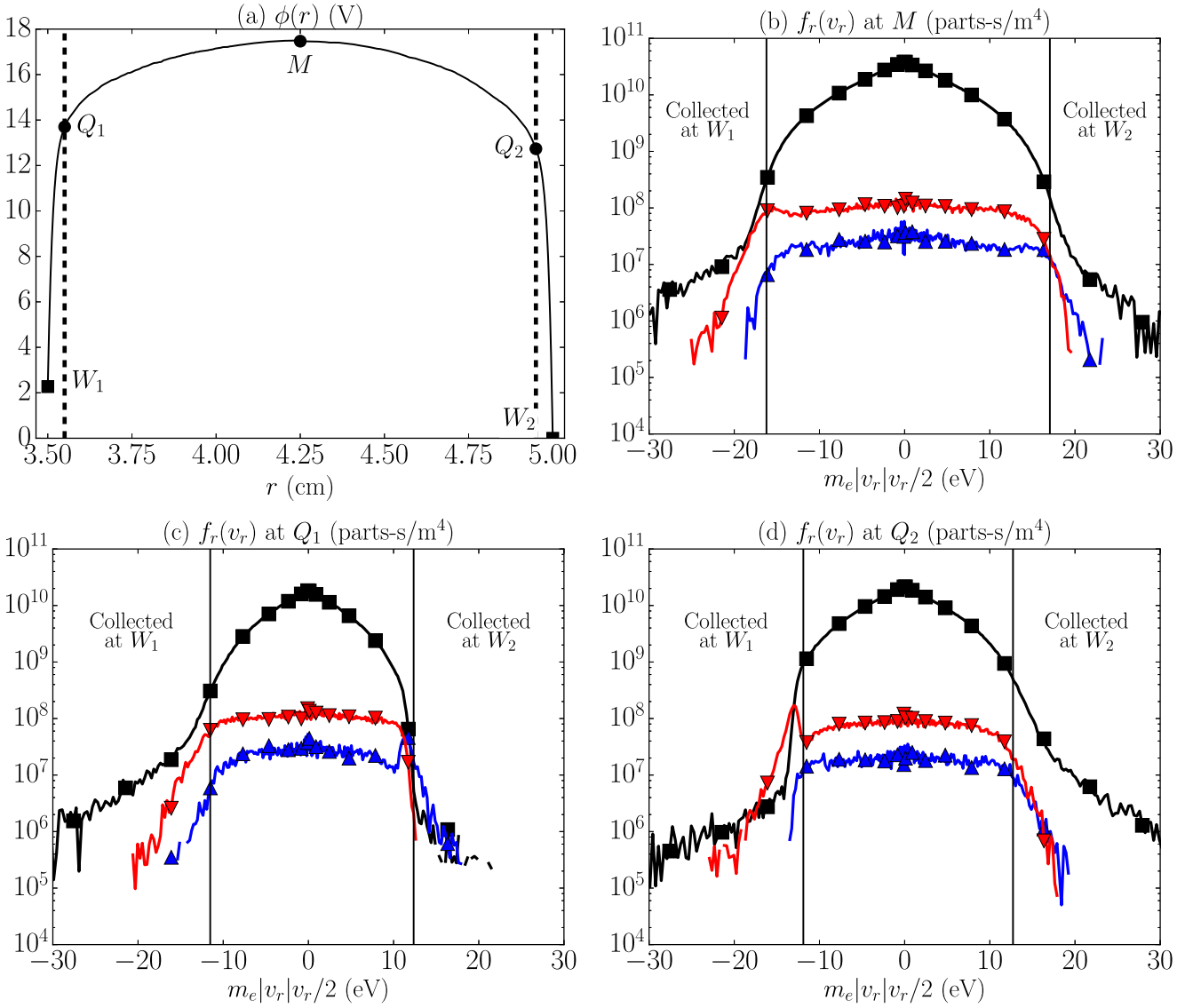

Figure 4. (a) Time-averaged (over last microseconds of simulation time) radial profile of the electric potential. Points M, Q_1, Q_2, W_1, and W_2 correspond to the channel mid-radius, sheath edges, and walls. (b)–(d) Radial VDF at nodes M, Q_1, and Q_2. Black, blue and red lines with squares, up triangles and down triangles correspond to the p-, s1- and s2-populations, respectively. The VDFs are accumulated over the last microsecond of simulation time.

tails, filled with wall-collectable electrons. Figures 4(c) and (d) show similar depletions of the VDF tails at points Q_1 and Q_2. In plot 4(c) the peak on the s1-VDF (blue line) corresponds to the electrons just emitted from W_1, which have acquired an electric potential energy $e\Delta\phi_{W_1Q_1} = 11.43$ eV when crossing the sheath. An equivalent explanation applies to the peak of the s2-VDF (red line) in plot 4(d), with an energy $e\Delta\phi_{W_2Q_2} = 12.74$ eV.

Beyond these peaks, the shape of the VDFs for secondary electrons at different locations is the consequence of their possible destinies. The most energetic ones are recollected after a single or double radial journey. The rest of them

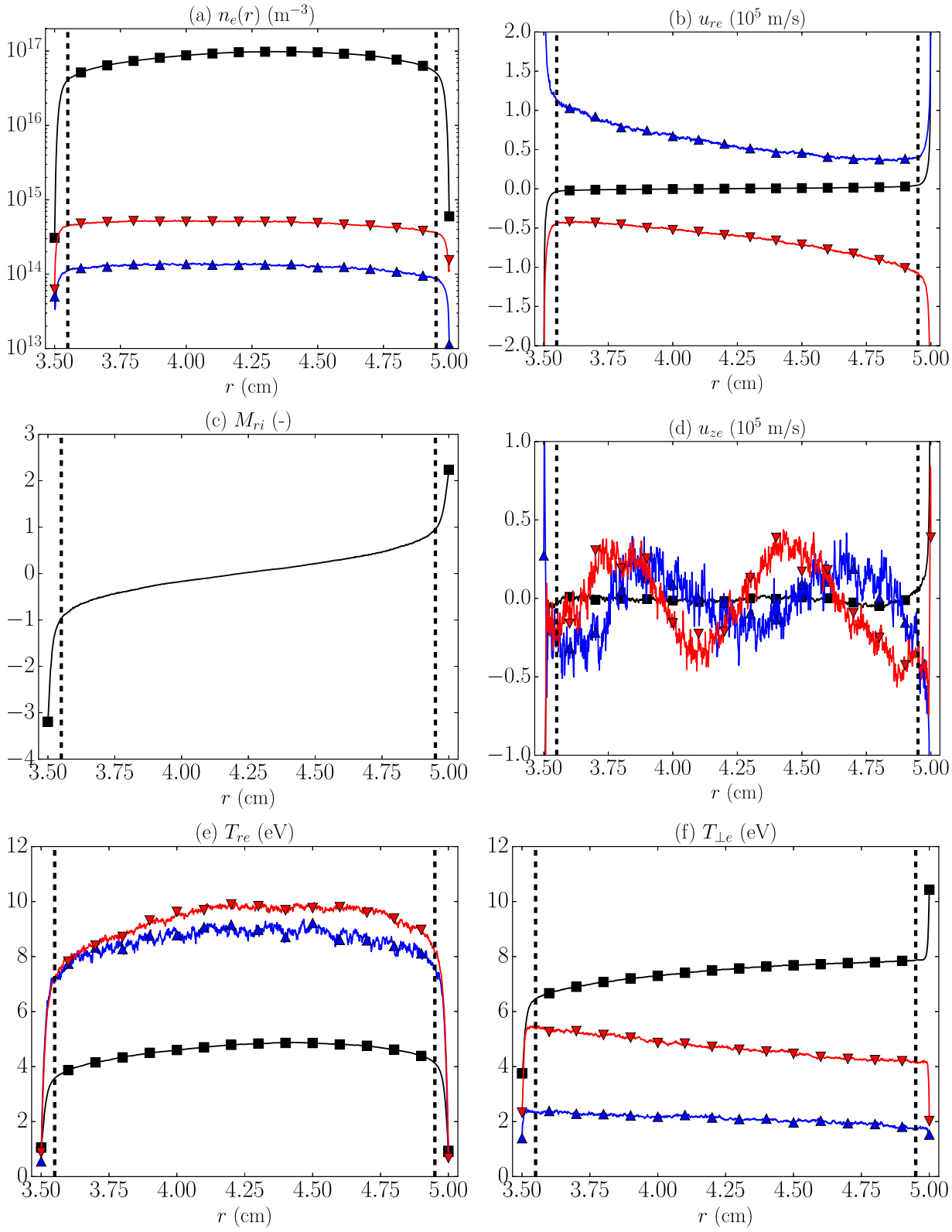

Figure 5. Steady-state radial profiles of macroscopic magnitudes for the different electron species and ions: (a) the electron particle density, (b) the electron radial velocity, (c) the ion radial Mach number, (d) the electron axial velocity, (e) the radial electron temperature, and (f) the perpendicular electron temperature. Black, blue and red lines with squares, up triangles and down triangles correspond to p-, s1- and s2-electron populations, respectively. Dashed vertical lines mark the approximate sheath edges. The curves are computed using the EVW algorithm with the last $N_k = 2 \cdot 10^5$ timesteps (equivalent to the last microsecond of simulation time).

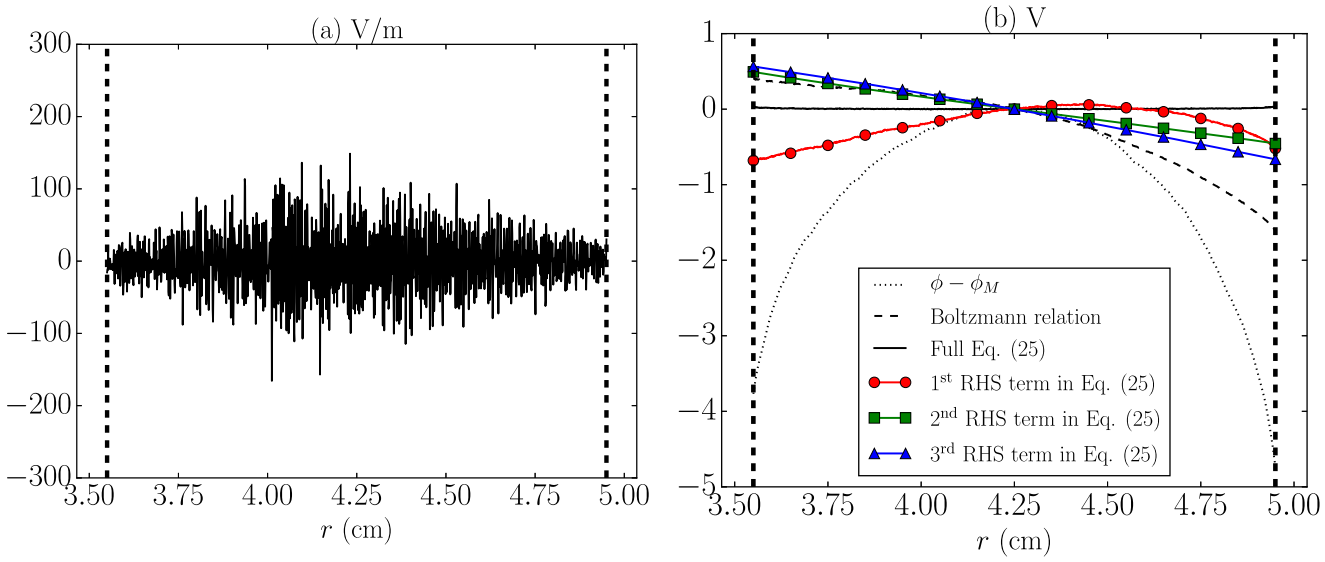

Figure 6. (a) Contribution of collisional and other minor effects to the local radial momentum balance of primary electrons, equation (24). (b) (dotted line) Electric potential profile relative to ϕ_M; (dashed line) Boltzmann relation, i.e. the left side of equation (25); (solid line) integrated radial momentum balance of primary electrons, i.e. the full equation (25); and contributions to the right side of equation (25): red circles correspond to the radial temperature non-uniformity term; green squares represent the temperature anisotropy contribution; and blue triangles stand for the centrifugal force. The macroscopic variables involved are computed through the EVW algorithm with the last $N_k = 2 \cdot 10^5$ timesteps (equivalent to the last microsecond of simulation time).

bounce radially, until collisions transfer them to the primary population. The SEE yield and the amounts of wall recollection and conversion to p-electrons determine the density and other macroscopic properties of secondary electrons. Table 2 provides detailed data on these processes: 60% and 63% of s1- and s2-electrons, respectively, are converted to p-electrons due to electron–neutral or large-angle Coulomb collisions, while the remaining fractions are recollected at the walls.

Table 2 also provides the currents of the different electron species to and from the walls. Most of the current to the walls comes from the p-population, which has a much higher density, as illustrated in figure 5(a). The most prominent result is that large asymmetries are found between walls in (i) the current exchanged at each of them, with a ratio of $|j_{e,2+}|/|j_{e,1-}| \simeq 1.59$, and (ii) the average true secondary electron yields, defined as

$$\langle \delta_{TS,1} \rangle = \frac{|j_{s1,1+}|}{|j_{e,1-}|} \approx 0.15, \quad \langle \delta_{TS,2} \rangle = \frac{|j_{s2,2-}|}{|j_{e,2+}|} \approx 0.29, \tag{23}$$

for each wall. Here and in table 2 subscripts 1 and 2 refer to both walls, and + and − to the direction of the radial velocity at the wall location. Since the two wall materials are the same, the difference in the effective SEE yields is due to a difference in the mean impacting energy per particle, E_w. This energy is obtained by dividing the net energy flux to a wall by the corresponding particle flux. Table 2 shows that $E_{wp,1} = 8.50$ eV and $E_{wp,2} = 16.16$ eV. In fact, these values are not far from twice the electron temperature, the mean impacting energy for a Maxwellian VDF.

Figure 5 plots the steady-state spatial profiles for the main macroscopic magnitudes. We focus the discussion here on the plasma bulk, since plasma magnitudes inside the steepened sheaths (such as the behavior of T_e) are generally not detailed in the conventional two-scale sheath analysis. Figure 5(a) plots the density profiles of the different electron populations, confirming the much lower densities of secondary electrons. In addition, a large asymmetry between the s1- and s2-population densities is observed. The lower s1 density is partially caused by the lower SEE yield from W_1.

Figure 5(b) plots the macroscopic radial velocity u_r for the three electron populations. Primary electrons behave as usual with inward and outward fluxes from (around) the channel mid-line M. The velocity increase inside the sheaths is just the consequence of the decreasing density there. Indeed, the same behavior is observed of the radial velocity of ions, figure 5(c), where $M_{ri} = u_{ri}(T_e/m_i)^{-1/2}$ is the radial Mach number, with m_i the ion mass. Observe that the sheath edges are placed at the ion sonic points.

Back to figure 5(b), the s1-electrons present a net outward radial velocity, indicating that their outward flow is slightly larger than the inward one, due to a larger recollection at W_2. The opposite situation happens to the s2-electrons. Notice that these radial velocities are just small drifts in the VDFs of the three populations: for instance, the energy corresponding to $u_r = 10^5$ m s^{-1} is ∼0.03 eV. The similar negative slope of du_r/dr for the s1- and s2-electrons is likely due to the net macroscopic effect of the magnetic mirror and the $E \times B$ contributions.

Figure 5(d) plots the macroscopic axial velocity, u_z, of the three electron populations. These velocities are practically zero except for the oscillations shown in secondary electrons which correspond to the net axial residual of their

gyromotion, giving rise to near-wall conductivity [13]. Although not shown here, ions present an average macroscopic velocity approximately equal to that assigned individually to their macroparticles when created. Very importantly, the simulations confirm that there are no secular effects on the axial flow of all populations and therefore there is no need to apply particle refreshing. (Nonetheless, in much longer simulations, collisional effects should yield a nonzero u_{ze} of the order of $u_{\theta e}$ divided by the Hall parameter.)

Figure 3(b) showed the mean temperatures of the three electron species. Now, figures 5(e) and (f) plot the radial (i.e. B-parallel) and perpendicular temperatures, unveiling significant anisotropy. For the three populations, it is found that $T_\theta \approx T_z \approx T_\perp$ and the anisotropy is the combined consequence of the electron magnetization and the depletion at the walls. Interestingly, and due to their very different dynamics, $T_r/T_\perp$ is lower than 1 for primary electrons and higher than 1 for secondary electrons. For instance, at point M one has $T_{rp,M}/T_{\perp p,M} \simeq 0.64$, $T_{rs1,M}/T_{\perp s1,M} \simeq 4.35$, and $T_{rs2,M}/T_{\perp s2,M} \simeq 2.08$. The temperature behavior of the primary electrons is a direct consequence of the partial depletion of their radial VDF tail. The trend $T_r/T_\perp > 1$ for secondary electrons would be due to their preferential radial bouncing, further enhanced by the fact that when they collide strongly they are transferred to the primary population.

Because of the very low density of secondary electrons, the radial potential profile of figure 5(a) is shaped almost exclusively by the p-population. Indeed, the complete macroscopic radial equilibrium for the p-electrons reads

$$e\frac{\partial\phi}{\partial r} - T_{rp}\frac{\partial \ln n_p}{\partial r} - \frac{\partial T_{rp}}{\partial r} + \frac{T_{\perp p} - T_{rp}}{r} + \frac{m_e u_{\theta p}^2}{r} = F_r'. \tag{24}$$

The first three terms on the left side are well known. The fourth one, where $\mathrm{d}\ln B/\mathrm{d}r = -1/r$ has been applied, is the magnetic mirror, which in the macroscopic formulation requires *both* a parallel magnetic gradient and a temperature anisotropy. The fifth term is the radial centrifugal force, coming from the $E \times B$ drift. On the right side F_r', plotted in figure 6(a), groups the contributions of collisions and the convective term $m_e u_{re}\partial u_{re}/\partial r$. Since F_r' has been computed from the sum of all the terms on the left side, its large oscillations are due to inaccuracies when computing spatial derivatives from noisy PIC profiles. The first two terms on the left side are the dominant ones, with a typical value of $\mathcal{O}(1000\ \mathrm{V\ m^{-1}})$. Therefore, we can conclude that F_r' and thus collisional and convection effects are marginal in the plasma response.

Neglecting F_r', the integration of equation (24) yields

$$\begin{aligned} &e\phi - e\phi_M - T_{rpM}\ln\frac{n_p}{n_{pM}} \\ &= \left[T_{rp} - T_{rpM} + \int_{r_M}^{r}\mathrm{d}r\,(T_{rp} - T_{rpM})\frac{\mathrm{d}\ln n_p}{\mathrm{d}r}\right] \\ &+ \int_{r_M}^{r}\mathrm{d}r\frac{T_{rp} - T_{\perp p}}{r} - \int_{r_M}^{r}\mathrm{d}r\frac{m_e u_{\theta p}^2}{r}. \end{aligned} \tag{25}$$

Here, the left side now groups the two terms of the isothermal Boltzmann relation, while the right side includes the effects of a non-uniform radial temperature, the magnetic mirror, and the centrifugal force. The different contributions are plotted in figure 6(b). This shows that the whole radial equilibrium of equation (25) is satisfied excellently; the three contributions of the right side are of the same order (see symbols at the sheath edges); and the sum of these three contributions introduces a correction of up to 30% (relative to $e\phi - e\phi_M$) in the Boltzmann relation.

The potential fall in a sheath is closely related to the electron currents to and from the walls. In particular, to fulfill the zero electric current condition, the lower the primary-electron current (because of VDF tail depletion), the lower the sheath potential fall. Ahedo and dePablo [8] treated this problem analytically by assuming a functional form of the p-VDF which fits well with the present results. They modeled partial depletion with a replenishment (via collisionality) parameter σ_t (not to be mistaken for the surface charge), which, in the end, measured the ratio between the actual potential fall and the one corresponding to a non-depleted Maxwellian population. For instance, for the inner wall W_1 it would be

$$\sigma_{t,1} = \frac{|j_{pW_1}|}{j_{ther,1}} \text{ with } j_{ther,1} = en_{pQ_1}\exp\left(-e\frac{\phi_{W_1Q_1}}{T_{pQ_1}}\right)\sqrt{\frac{T_{pQ_1}}{2\pi m_e}}, \tag{26}$$

and a similar definition applies to the outer wall. In our simulation, the p-tail replenishment ratios are rather low, $\sigma_{t,1} \simeq 0.04$ and $\sigma_{t,2} \simeq 0.05$, which seem reasonable with the weak electron collisionality. If instead of the total temperature T_p, the radial temperature T_{rp} were used in the definition of j_{ther}, it would still be $\sigma_{t,1} \simeq 0.15$ and $\sigma_{t,2} \simeq 0.19$.

A final point to comment is that, in the present ionization-controlled model with no axial (i.e. external) injection of particles along the simulation, the mean steady-state electron temperature is totally intrinsic to the model and its parameters. Indeed, simulations started with different values of T_{e0} between 1 and 20 eV have led to the same final temperatures shown here. This final temperature comes from the energy balance

$$\begin{aligned} &P_{sinks} = P_{sources},\quad P_{sinks} \simeq P_{inel} + P_{wall,t}, \\ &P_{sources} \simeq P_{elec} + P_{wall,f}, \end{aligned} \tag{27}$$

where P_{inel} denotes the losses due to inelastic processes (ionization and excitation), $P_{wall,t}$ denotes the losses due to electron collection at the walls, $P_{wall,f}$ denotes the gains due to electron emission at the walls, and P_{elec} is the energy transmitted to the electrons by the electric field. The values of these terms are in table 2: $P_{wall,f}$ is negligible and P_{inel} and $P_{wall,t}$ are of the same order.

In the opposite case of an axially controlled radial discharge, i.e. with $S_{axial,j} \gg S_{ioniz}$ in equation (1), the mean T_e would be dependent mainly on the temperature of the macro-electrons continuously injected through $S_{axial,j}$. Therefore, while the temperature anisotropy of the primary population and

possibly the temperatures of the secondary populations are relevant results of a 1Dr model, the mean value of T_e is partially arbitrary. Indeed, in the complete HET discharge, T_e is determined basically by the axial dynamics, through the discharge voltage, the Joule heating, and the ionization and wall losses.

5. Conclusions

The annular model and related PIC/MCC code of a given radial section of the acceleration region of a HET has been built on a previous one by Taccogna [16]. The main numerical improvements and conclusions are as follows. First, in an ionization-controlled discharge we cannot fix both the mean neutral density and the mean plasma density. Second, fixing the mean plasma density and adjusting the neutral density along the simulation is a preferable method in terms of optimizing the PIC implementation. Third, the secular growth of ion axial energy and the subsequent refreshing of macroions is avoided by canceling the ion axial acceleration. And fourth, a time-extended volumetric weighting algorithm is implemented, which improves very substantially the weighting of macroscopic magnitudes of the minor species (here the true secondary electrons), while not affecting the major species (here the primary electrons and the ions).

On the physical side the main contributions are as follows. First, because of the weak collisionality (dominated by elastic electron–neutral collisions), the VDF of primary electrons presents an important depletion of the high-radial-energy tails, leading to a radial-to-perpendicular temperature anisotropy ratio of about $2/3$ in the simulation discussed here. Second, the true secondary electrons are partially converted to primary electrons (after a strong collision) and partially recollected by the walls, in a proportion of about 40%–60%. The resulting density of the secondary electrons is very low, thus only slightly affecting the shape of the electric potential profile. Besides, secondary electrons maintain a low radial drift velocity and a radial-to-perpendicular temperature ratio higher than one. Third, the replenishment ratio of the high-radial-energy tail of primary electrons is low, which leads to a reduced sheath potential fall. Fourth, the electric potential profile in the (quasineutral) plasma bulk comes from a radial momentum equilibrium which goes beyond the classical Boltzmann relation and incorporates non-negligible contributions of (i) the radial temperature gradients, (ii) the magnetic mirror, and (iii) the centrifugal force. This macroscopic magnetic mirror effect combines the temperature anisotropy and the cylindrical divergence of the magnetic field. The relevance of the centrifugal force stands out since it is disregarded in macroscopic models invoking the zero electron inertia limit, but this assumption does not take into account the subtle detail that $m_e u_{\theta e}^2/2r$ is in a HET plasma much larger than $m_e u_{re}\partial u_{re}/\partial r$. And fifth, the above cylindrical effects introduce significant asymmetry in (i) the plasma profiles with respect to the mid-radius and (ii) the magnitudes related to plasma–wall interaction, such as the collected currents and the mean impact energies, and thus the resulting SEE yields.

While the present work is devoted to improvements of the 1Dr code and the capabilities it has to analyze kinetic and macroscopic plasma responses, further work will deal with a parametric investigation on the trends and features found in the simulation analyzed here. This should yield scaling laws among input and output parameters, which will provide a solid characterization of 1Dr discharge. Besides, some of these laws could be implemented as auxiliary models in HET hybrid codes, which use a macroscopic formulation of the electron popula-tion; one example is the replenishment ratio of the VDF for sheath calculations. A particularly interesting parametric investigation is on increasing the axial electric field in order to reach electron azimuthal velocities above the electron thermal velocity. This would allow one to analyze the reported trans-ition from a stable steady-state discharge to an instability-saturated one. A second prominent investigation is on plasma response in the presence of a non-fully-radial magnetic field, which is expected to largely modify the tails of the electron VDFs and the temperature anisotropy.

Acknowledgments

The work at UC3M was supported by the CHEOPS project, funded by the European Union's Horizon 2020 Research and Innovation Programme, under Grant Agreement 730135. Additional support came from Spain's National Research and Development Plan (Project ESP2016-75887). F T was supported by the Apulia Space Project (grant PON03PE_00067_6).

References

[1] Ahedo E 2011 Plasmas for space propulsion *Plasma Phys. Control. Fusion* **53** 124037
[2] Goebel D M and Katz I 2008 *Fundamentals of Electric Propulsion: Ion and Hall Thrusters* (New York: Wiley)
[3] Jahn R G 1968 *Physics of Electric Propulsion* (New York: McGraw-Hill) (reprinted by Dover)
[4] Barral S, Peradzynski Z, Makowski K and Dudeck M 2003 An alternative theory of transit-time oscillations in Hall thrusters *Proc. 28th Int. Electric Propulsion Conf., Toulouse, France* paper IEPC 03–335, Electric Rocket Propulsion Society, https://erps.spacegrant.org
[5] Ahedo E and Parra F I 2002 Model of radial plasma-wall interactions in a Hall thruster *Proc. 38th Joint Propulsion Conf., Indianapolis, IN,* Paper AIAA 2002–4106, American Institute of Aeronautics and Astronautics, https://www.aiaa.org/
[6] Ahedo E, Gallardo J M and Martínez-Sánchez M 2003 Effects of the radial-plasma wall interaction on the axial Hall thruster discharge *Phys. Plasmas* **10** 3397–409
[7] Ahedo E and Parra F I 2005 Partial trapping of secondary electron emission in a Hall thruster plasma *Phys. Plasmas* **12** 073503

[8] Ahedo E and de Pablo V 2007 Combined effects of electron partial thermalization and secondary emission in Hall thruster discharges *Phys. Plasmas* **14** 083501

[9] Sydorenko D, Smolyakov A, Kaganovich I and Raitses Y 2006 Modification of electron velocity distribution in bounded plasmas by secondary electron emission *IEEE Trans. Plasma Sci.* **34** 815–24

[10] Kaganovich I D, Raitses Y, Sydorenko D and Smolyakov A 2007 Kinetic effects in a Hall thruster discharge *Phys. Plasmas* **14** 057104

[11] Birdsall C K 1991 Particle-in-cell charged particle simulations, plus Monte Carlo collisions with neutral atoms, PIC-MCC *Trans. Plasma Sci.* **19** 65–85

[12] Hockney R W and Eastwood J W 1988 *Computer Simulations Using Particles* (Bristol: Hilger)

[13] Bugrova A I, Morozov A I and Kharchevnikov V K 1990 Experimental studies of near wall conductivity *Fiz. Plazmy* **16** 1469–81

[14] Wang H, Campanell M, Kaganovich I and Cai G 2014 Effect of asymmetric secondary emission in bounded low-collisional E×B plasma on sheath and plasma properties *J. Phys. D: Appl. Phys.* **47** 405204

[15] Taccogna F, Longo S, Capitelli M and Schneider R 2007 Particle-in-cell simulation of stationary plasma thruster *Contrib. Plasma Phys.* **47** 635–56

[16] Taccogna F, Longo S, Capitelli M and Schneider R 2008 Surface-driven asymmetry and instability in the acceleration region of a Hall thruster *Contrib. Plasma Phys.* **48** 1–12

[17] Taccogna F, Schneider R, Longo S and Capitelli M 2008 Kinetic simulations of a plasma thruster *Plasma Sources Sci. Technol.* **17** 024003

[18] Furman M A and Pivi M T F 2002 Probabilistic model for the simulation of secondary electron emission *Phys. Rev. ST Accel. Beams* **5** 124404

[19] Nanbu K 2000 Probability theory of electron-molecule, ion-molecule, molecule-molecule, and Coulomb collisions for particle modeling of materials processing plasmas and gases *IEEE Trans. Plasma Sci.* **28** 971–90

[20] Nanbu K 2000 Simple method to determine collisional event in Monte Carlo simulation of electron-molecule collision *Jpn. J. Appl. Phys.* **33** 4752–3

[21] Surendra M, Graves D B and Morey I J 1990 Electron heating in low-pressure RF glow discharges *Appl. Phys. Lett.* **56** 1022–4

[22] Nanbu K 1997 Theory of cumulative small-angle collisions in plasmas *Phys. Rev. E* **55** 4642–52

[23] Nanbu K and Yonemura S 1998 Weighted particles in Coulomb collision simulations based on the theory of a cumulative scattering angle *J. Comput. Phys.* **145** 639–54

[24] Bobylev A V and Nanbu K 2000 Theory of collision algorithms for gases and plasmas based on the Boltzmann equation and the Landau-Fokker-Plack equation *Phys. Rev. E* **61** 4576–86

[25] Wang C, Lin T, Caflisch R, Cohen B I and Dimits A M 2008 Particle simulation of Coulomb collisions: comparing the methods of Takizuka & Abe and Nanbu *J. Comput. Phys.* **227** 4308–29

[26] Birdsall C K and Langdon A B 1991 *Plasma Physics via Computer Simulation* (Bristol: Hilger)

[27] Verboncoeur J P 2001 Symmetric spline weighting for charge and current density in particle simulation *J. Comput. Phys.* **174** 421–7

[28] Santos R, Ahedo E and Santos R 2009 Implementation of the kinetic Bohm condition in a Hall thruster hybrid code, Paper AIAA 2009-4913, American Institute of Aeronautics and Astronautics, https://www.aiaa.org/

[29] Ahedo E, Santos R and Parra F I 2010 Fulfillment of the kinetic Bohm criterion in a quasineutral particle-in-cell model *Phys. Plasmas* **17** 073507

[30] Press W H, Teukolsky S A, Vetterling W T and Flannery B P 2001 *Numerical Recipes in Fortran 77: The Art of Scientific Computing* (New York: Cambridge University Press) Available online: http://numerical.recipes/

[31] Szabo J J Jr. 2001 Fully kinetic numerical modeling of a plasma thruster *PhD Thesis* (Cambridge, MA: Massachuchusetts Institute of Technology)